

Millimeter-Wavelength Dual-Polarized Lens-Absorber-Coupled Ti/Al Kinetic Inductance Detectors

Alejandro Pascual Laguna, Victor Rollano, Aimar Najarro-Fiandra, David Rodriguez, Maria T. Magaz, Daniel Granados, Alicia Gomez

Abstract—This work presents Ti/Al bi-layer Microwave Kinetic Inductance Detectors (MKIDs) based on lens-coupled spiral absorbers as the quasi-optical coupling mechanism for millimeter-wavelength radiation detection. From simulations, the lens-coupled absorbers provide a 70% lens aperture efficiency in both polarizations over an octave band with a spiral array absorber and over 10% relative bandwidth with a single spiral. We have fabricated and measured two devices with bare Ti/Al MKIDs: a 3×3 cm chip with 9 pixels to characterize the optical response at 85 GHz of the two variations of the absorber; and a large format demonstrator with 253 spiral-array pixels showing potential towards a large format millimeter-wavelength camera. We find a sensitivity of $1 \text{ mK}/\sqrt{\text{Hz}}$ and a detector yield of 95%.

Index Terms—Absorber, dual-polarization, lens, MKID, millimeter-wavelength, Ti/Al

I. INTRODUCTION

MICROWAVE Kinetic Inductance Detectors (MKIDs) [1] are showing very high sensitivities at far-infrared [2], [3], mid-infrared [4], [5], and near infrared to optical wavelengths [6]–[8]. At millimeter-wavelengths, where coherent detectors have traditionally dominated, direct detectors like MKIDs are also becoming very competent for various astronomical applications [9]–[15] and are even being considered for photon-mediated dark matter detection experiments [16]. However, in order for MKIDs to sense the low energy end of the millimeter wavelengths, low critical temperature (T_c) superconductors must be employed. Thin Ti/Al multilayers relying on the proximity effect are most actively being investigated [17]–[19], but other low T_c superconductors like Hf, Ta or Mo could also be considered [20].

Manuscript received September 26, 2025; revised Month dd, yyyy. The authors acknowledge support from grants JDC2023-051842-I, PID2022-137779OB-C41, PID2022-137779OB-C42 funded by the Spanish MCIN/AEI/10.13039/501100011033, by the EU “NextGenerationEU”/PRTR and by the “ERDF A way of making Europe”. IMDEA Nanoscience acknowledges financial support from the “Severo Ochoa” Programme for Centres of Excellence in R&D (CEX2020-001039-S); and CAB from the CSIC Research Platform PTI-001, from “Tecnologías avanzadas para la exploración del Universo y sus componentes” (PR47/21 TAU-CM) and Mad4Space-TEC-2024/TEC-182 projects funded by Comunidad de Madrid, by “NextGenerationEU”/PRTR. (Corresponding authors: A. Pascual Laguna, A. Gomez)

Alejandro Pascual Laguna, Victor Rollano, Aimar Najarro-Fiandra, David Rodriguez, Maria T. Magaz and Alicia Gomez are with Centro de Astrobiología (CSIC-INTA), Torrejón de Ardoz, 28850, Spain. (emails: apascual@cab.inta-csic.es; agomez@cab.inta-csic.es;)

D. Granados is with the Instituto Madrileño de Estudios Avanzados en Nanociencia (IMDEA Nanociencia), 28049, Madrid, Spain.

Color versions of one or more figures in this article are available at <https://doi.org/nn.nnnn/TASC.yyyy.nnnnnn>.

Digital Object Identifier nn.nnnn/TASC.yyyy.nnnnnn

Employing low T_c superconductors enables the detection of low energy radiation provided it can reach the detector. To this end, the quasi-optical design must be optimized according to the scientific scenario. Although absorber-coupled detectors generally provide worse angular resolution than antenna-coupled ones [21], [22], absorbers are typically easier to fabricate and are more resilient to fabrication tolerances due their insensitivity to phase errors. As opposed to fill-arrays of bare absorbers, lens-coupled absorbers allow a slight decoupling of a proper quasi-optical design with the foreoptics from the detector sensitivity optimization [5].

In this article, we propose a broadband lens-absorber-coupled Ti/Al MKID with similar sensitivity in both polarizations, which could be used in millimeter-wavelength polarimetric instruments with the aid of rotating half-wave plates or polarizers [12]. We report the cryogenic characterization of the detector optical sensitivity at 85 GHz, and showcase a large millimeter-wavelength MKID camera prototype.

II. LENS-COUPLED ABSORBER WITH A BROADBAND DUAL-POLARIZED RESPONSE

Ultrasensitive broadband dual-polarized absorber-coupled detectors [4], [5], [23] are key to maximize the observing capabilities of future astronomical observatories. These detectors are typically made of Al because of its ease of fabrication and long quasi-particle lifetimes. However, Al-based absorbers are very difficult to fabricate for sub-millimeter wavelengths, where features become sub-micron to compensate the low impedance of Al. At millimeter wavelengths however, this becomes practical and there is more freedom in the design space. To this end, we propose a Ti/Al ($R_s \approx 1 \Omega/\square$) absorber consisting of a square double spiral unit cell, with $3 \mu\text{m}$ -wide arms spiraling inwards and outwards connected in series in the middle. Figure 1 depicts two lumped-element resonator designs, where the capacitor is an interdigitate arrangement, and the inductor is based on the proposed double spiral unit cell in two variations: (a) with a single spiral and (b) with an array of 4×4 spirals whose rows are connected in parallel to avoid self-resonances. The resonators are on a slab of Si backed with a ground plane, serving both as a quarter-wavelength backing reflector for millimeter wavelengths and for the ground plane of the microstrip microwave readout line.

Figure 2 shows each spiral absorber placed at the lower focus of an extended hemispherical Si lens with a clear aperture diameter of 5 mm and a radius-normalized extension length of $L/R = 0.39$ to synthesize an ellipsoidal shape [24]. The single spiral absorber in (a) was coupled to an $f_{\#} = 0.63$

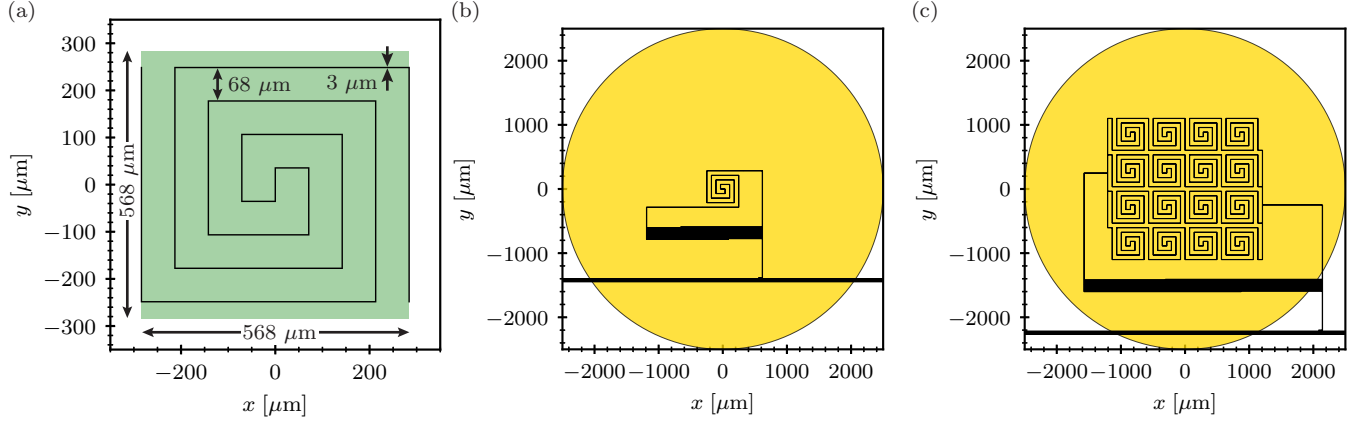


Fig. 1. Panel (a) shows the absorbing spiral and its dimensions, where the green square is just a visual aid to show the extend of the unit cell. Panel (b) shows a lumped element resonator with a single spiral as inductive element. Panel (c) shows a resonator with a 4×4 spiral array as inductive element. Both designs use an interdigitated capacitor. The yellow circle is the footprint of the lens clear aperture on top of each MKID.

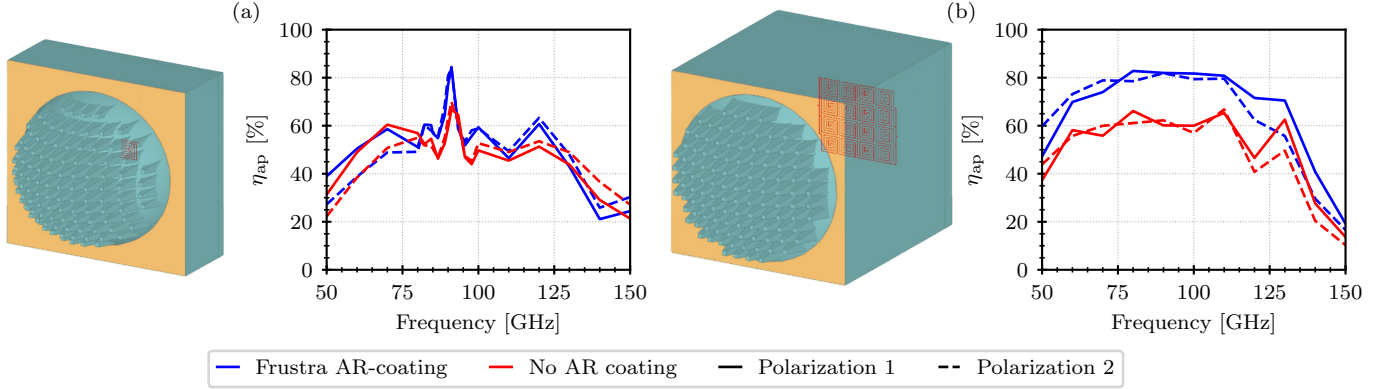


Fig. 2. Geometry and aperture efficiency for two orthogonal polarizations for (a) the lens-coupled double-spiral and (b) the lens-coupled double-spiral 4×4 array, in both cases analyzed with and without broadband AR coating. The absorbers (in red) are at the lower focus of the synthesized elliptical lens. The frustras are not conformal to the lens shape to be able to use current capabilities in laser ablation technology [25]. The orange sheet has a sheet impedance to perfectly absorb a free-space plane and are included in the simulations to limit the input power to the lens clear aperture.

lens to maximize the power collection while avoiding the deepest lens configuration at $f_{\#} = 0.54$, where the lens radius coincides with the clear aperture diameter. This results in a focal field sampling of $1\lambda_{\text{Si}}f_{\#}$, where λ_{Si} is the wavelength in silicon. On the other hand, the 4×4 spiral-array in (b) was coupled to an $f_{\#} = 1.2$ lens to maximize the power coupling with the absorber lateral dimension being $2\lambda_{\text{Si}}f_{\#}$.

To avoid reflections at the silicon-vacuum interface, the lens top is shaped with vertical (non-conformal) frustras to create a broadband anti-reflection (AR) coating suitable for cryogenic temperatures [25]. The design and performance of the AR-coating is reported in Fig. 3 for a broadside plane-wave incidence. The performance of the two lens-coupled absorber designs was simulated with CST Studio Suite [26] in terms of their broadside plane-wave response for two orthogonal polarizations. In order to restrict the plane wave to the lens clear aperture we added a perfectly absorbing sheet with the free-space impedance. The results of both designs are shown in Fig. 2 indicating a lens-aperture efficiency η_{ap} for both polarizations of more than 70% for about 10% relative bandwidth for the single spiral absorber in (a), and for an

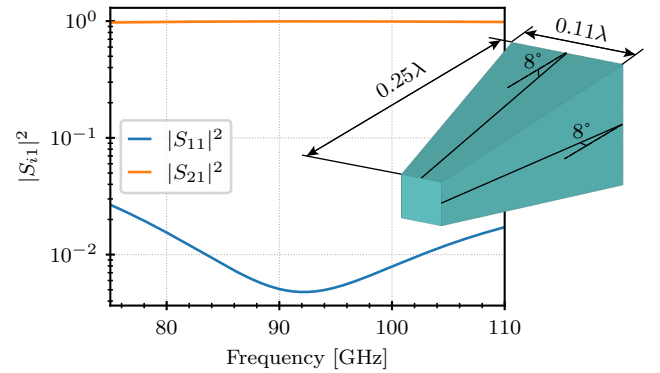


Fig. 3. Broadside plane-wave response of the frustra AR-coating unit cell shown in the inset. Port 1 is above the frustra and port 2 is below, embedded in silicon. The dimensions are given as function of the free-space wavelength at the central frequency of operation, here 92.5 GHz. These dimensions are achievable with current laser ablation technology.

octave for the spiral array in (b).

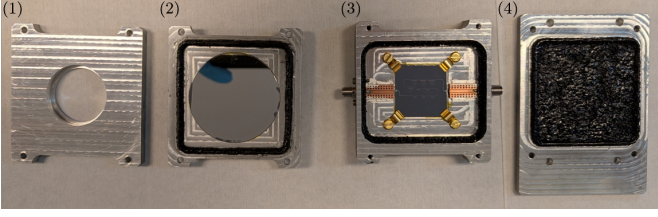


Fig. 4. Photograph of the light-tight Al holder for 3×3 cm chips. The different parts of the holder are: (1) the top lid with an aperture stop of $\varnothing 3$ cm, (2) the lid holding a 85 GHz $\varnothing 2$ " Fabry-Pérot band-pass filter, (3) the part holding the 9 MKID chip wire-bonded to the grounded coplanar waveguide PCB launchers interfacing with the SMA connectors, and (4) the bottom lid to close the assembly. The bottom lid and the joins of the parts are blackened with a thin stray-light absorbing layer.

III. FABRICATION

We have fabricated two lens-less MKID devices: a small 3×3 cm chip for testing the new designs, comprising 5 spiral array detectors and 4 single spiral detectors; and a large format demonstrator with 253 detectors spiral array detectors. The small chip was made from a 2" 280 μm -thick moderate resistivity ($\rho \gtrsim 1000 \mu\Omega \cdot \text{cm}$) double-side-polished float-zone silicon wafer, and the large format demonstrator was instead made from a 4" wafer with very high resistivity ($\rho \gtrsim 10\,000 \mu\Omega \cdot \text{cm}$). The recipe is the same for both devices. We first sputter-deposit on the wafer 10 nm of Ti and then, without breaking the vacuum in the sputter chamber to avoid oxidation, we add 20 nm of Al. This layer is patterned to define the resonators and readout line using mask-less laser lithography on a negative resist (AZ nLOF 2070), which is developed in AZ developer. The exposed Ti/Al is then subsequently wet-etched with TechniEtch A180 to attack Al and TechniEtch TBR19 to attack Ti. To make the ground plane we first protect the frontside with resist and then deposit 200 nm of Al in the backside of the wafer. The fabricated devices can be seen, already assembled in their chip holders, in Figs. 4 and 5. Future experiments will include a Si lens array that is aligned and glued to the detector wafer. The lenses, including the frustra AR-coating, will be manufactured from a monolithic Si wafer by means of laser ablation [25]. The glueing of the lens array and device wafers will be done with either a lithographic glue like PermiNex[®] or a high viscosity glue like epoxy 2216 [2].

To assess the Ti/Al bilayer properties, we performed a 4-point DC resistance measurement of a 4165.7 squares-long 15/11 nm-thick Ti/Al wire co-fabricated with the small device chip shown in Fig. 4. The sheet resistance as a function of temperature is given in Fig. 6, which is $1.1 \Omega/\square$ just above the superconducting gap and corresponds to an effective normal state resistivity of $\rho = 3.31 \mu\Omega \cdot \text{cm}$. The critical temperature is $T_c = 800$ mK, resulting in a gap frequency of $f_{\text{gap}} = 2\Delta_0/h \approx 3.52k_B T_c/h \approx 59$ GHz, where k_B is Boltzmann's constant and h is Planck's constant. Using the full Mattis-Bardeen equations [27] for the complex conductivity and the dirty limit sheet impedance we estimate a kinetic inductance of 1.9 pH/ \square .

To perform a controlled optical response characterization of the detectors, we have fabricated the Al chip holder depicted in

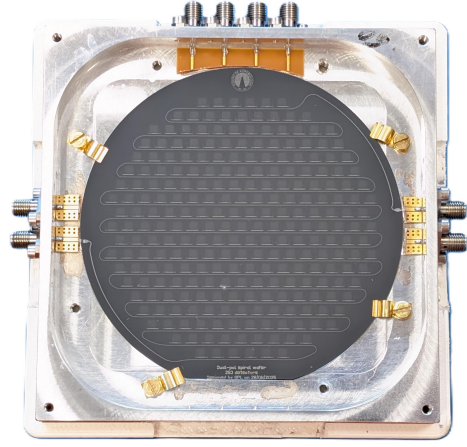


Fig. 5. Photograph of the large format demonstrator fabricated on a 4" wafer and hosting 253 MKIDs. The device is placed on an Al holder, where only two of its SMAs connectors are employed to read out the device in a frequency-multiplexed fashion.

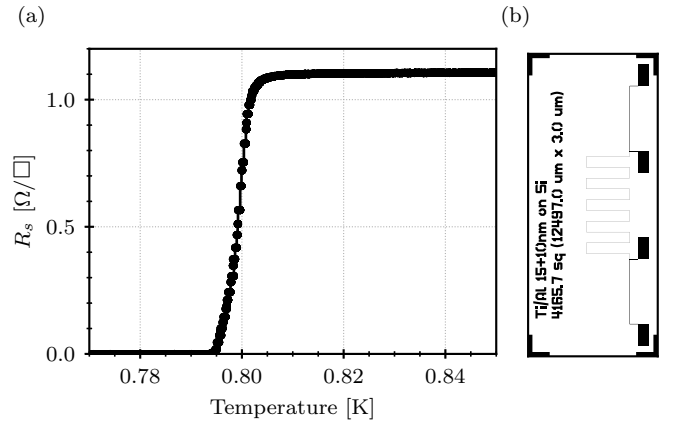


Fig. 6. Panel (a) shows the measured sheet resistance of a bi-layer of 11 nm-thick Ti and 19 nm-thick Al. Close to the gap, the normal state sheet resistance is $1.1 \Omega/\square$ and the resistivity is $3.3 \mu\Omega \cdot \text{cm}$. The critical temperature is approximately 800 mK. Panel (b) shows the layout of the chip employed to measure the resistance.

Fig. 4, where millimeter-wavelength radiation is only allowed through a $\varnothing 3$ cm aperture. All interfaces susceptible of letting stray radiation inside the holder have been carefully engineered to make radiation find a thin absorbing layer composed of a mixture of 1 mm SiC grains, Stycast 2850FT and carbon black powder [2], [28]. Furthermore, in order to ensure the probing of millimeter-wavelength radiation and eventually obtaining the optical efficiency of these multi-moded detectors, we have also designed and fabricated a 85 GHz Fabry-Pérot band-pass filter with the dimensions in Fig. 7. It consists of two highly reflective metallic layers separated by a half-wavelength medium. To this end, we use a standard 2" 525 μm -thick high-resistivity ($\rho \gtrsim 1000 \mu\Omega \cdot \text{cm}$) double-side-polished float-zone silicon wafer. We start by covering the wafer with resist in the backside to protect it for further processing. We subsequently deposit AZ1505 positive resist, and pattern the filter lines with mask-laser lithography. After developing the resist, we evaporate by e-beam 5 nm of Ti to promote adhesion and,

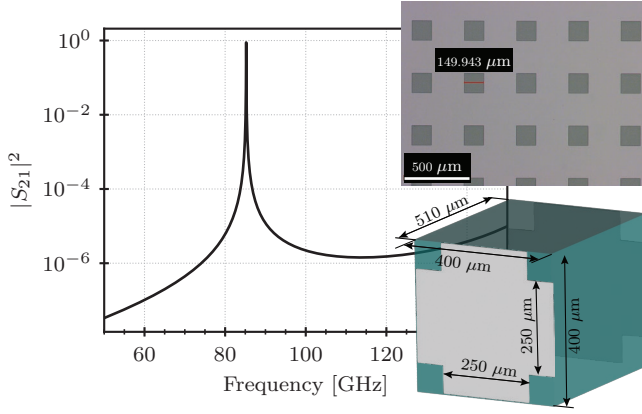


Fig. 7. Simulated broadside plane-wave transmission of the perfectly-conducting Fabry-Pérot band-pass filter with the unit cell shown in the lower inset. The layer below is exactly the same as the layer above. The upper inset shows an optical microscope photograph of the fabricated device.

without breaking the vacuum of the evaporator chamber, a 100 nm-thick film of Nb. We finally perform lift-off, thereby removing the metal in the filter gaps. The same steps are repeated on the backside of the wafer with front-to-back alignment using the front and rear cameras of the laser writer. The fabricated filter can be seen mounted in place in the part (2) of the chip holder in Fig. 4.

IV. OPTICAL CRYOGENIC CHARACTERIZATION

The small chip device was cooled to 100 mK, and we performed an optical characterization of the two resonator types against a temperature-calibrated blackbody radiator. The blackbody is clamped to the 4K stage of our cryostat and placed directly in front of the chip under test. The blackbody radiation is filtered by a 110 GHz low-pass filter from QMCI [29], and our own 85 GHz Fabry-Pérot band-pass filter. The blackbody brilliance for the temperatures under consideration T_{BB} and the filter stack transmission $F(f)$ are shown in Fig. 8(a). To obtain the sensitivity of our detectors, we employ a methodology described by Baselmans *et al.* [2]: we stabilize the blackbody at a temperature T_{BB} , measure the power spectral density (PSD) of the observable variable (x), sweep the temperature around T_{BB} to obtain the responsivity with respect to the blackbody temperature dx/dP_{BB} . Because we still do not have cryogenic transmission measurements of our filters, we only report the response with respect to the blackbody temperature. As can be seen in the PSDs in Fig. 8(b), our detectors are largely dominated by $1/f$ noise mostly due to inadequate thermal and mechanical anchoring in our setup. Despite this excess setup noise we are working on improving, we can clearly see a white spectrum with a roll-off increasing with loading, evidence of quasi-particle generation-recombination noise [30]. Furthermore, in Fig. 8(c) we report the optical response by means of the frequency shift δf_r observable as a function of the blackbody temperature T_{BB} . Our first estimates for 85 GHz radiation indicate a frequency responsivity of $\delta f_r/\delta T_{BB} \sim 1 \text{ Hz/mK}$ and thereby a Noise Equivalent Temperature (NET) of order $1 \text{ mK}/\sqrt{\text{Hz}}$ for both types of detectors at 1 kHz audio frequency.

V. LARGE FORMAT DEMONSTRATOR

Due to the adequate measured optical response of both detector types shown in section IV, and the very good simulated performance of the 4×4 spiral array one described in section II, we designed and fabricated a large format demonstrator with this large pixel configuration. One of the biggest challenges to array many detectors in a single readout line is cross-talk between pixels. To mitigate it, the distribution of MKIDs in the wafer follows a shuffling algorithm, which is illustrated in Fig. 9, and is similar to other encodings in the literature [31], [32]. In this shuffling strategy, the resonance frequencies are split in four contiguous sub-groups across the readout bandwidth and are distributed in cells of four physically neighboring resonators, each of one sub-group. These cells spiral outwards from the array center while rotating the sub-group elements allocation within the cell in such a way that spectrally adjacent resonators are either two elements apart vertically and one horizontally (in a square lattice) or vice versa.

To quantify the level of cross-talk, we have simulated pairs neighboring resonators where one is kept unaltered and the other is slightly de-tuned [31], [32]. As depicted in Fig. 10(a), the pairs of resonators analyzed are separated by a 5 mm pitch either laterally or transversely due to the hexagonal packing employed to maximize the array filling factor. Due to the electromagnetic interaction, the resonators become coupled and affect each other. To assess the cross-talk level, we have introduced a small change δl_{trim} affecting the length of the fingers of the interdigitated capacitor of one resonator. The frequency separation between the resonances of the coupled resonators is illustrated in Fig. 10(b). As expected, even when the resonators are exactly the same ($\delta l_{\text{trim}} = 0$), the two resonances are slightly different. The cross-talk level can be calculated from the ratio of resonance frequency change with respect to the nominal isolated resonator of the fixed resonator over the one for the varying one. The cross-talk level is plotted in Fig. 10(c) as a function of the design frequency spacing Δf_r^{des} . The resonators cross-talk less than 10% if they are spaced more than 1 MHz, in both orientations for a 5 mm pitch. If the resonators are placed under the Si lens array, the cross-talk decreases to $\sim 1\%$ for 1 MHz. According to this, only resonators closer than 1 MHz could incur about 10% cross-talk, which by design are 5% of them as shown in Fig. 9.

The large format demonstrator was measured at 100 mK bath temperature, but we limited the characterization to the microwave readout transmission. As depicted in Fig. 5(a), we found 241 resonators out of 253, resulting in a 95% detector yield; of which 39 are deemed unusable due to their close proximity (less than 20 half-power bandwidths) to a neighboring resonance. As shown in Fig. 5(b) and (c) The measured resonance frequencies f_r^{meas} were found to deviate from the design values f_r^{des} an average of 5.0% and with a standard deviation of 5.8%. The trend of measured resonance frequencies with respect to the designed ones is reminiscent of the cross-talk analysis shown in [31]. However, the seemingly large remanent cross-talk between resonators is likely caused by fabrication imperfections (film thickness

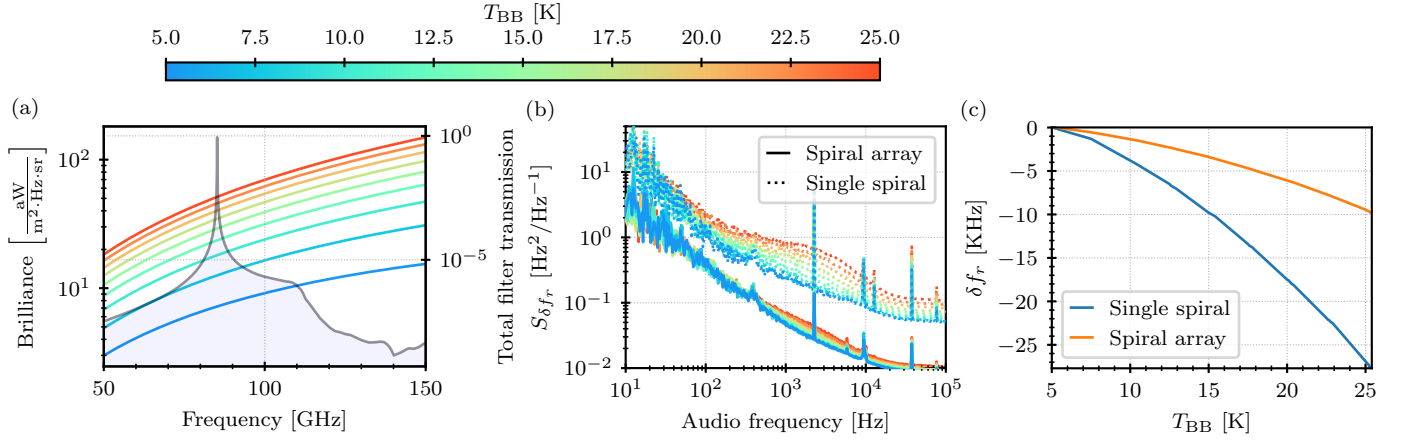


Fig. 8. Panel (a) shows the brilliance at the investigated blackbody temperatures and the total filter stack-up transmission. Panel (b) shows the PSD in the resonance shift coordinate $S_{\delta f_r}$ for both a single spiral detector and a spiral array detector of the small chip at 100 mK bath temperature. Despite the large $1/f$ noise, quasi-particle generation recombination noise is visible for both detectors. The difference in the high frequency white noise level is due to the very different quality factor of the particular resonators of choice, but the power level at the chip is -85 dBm for both. Panel (c) shows the response of these two detectors as a function of blackbody temperature.

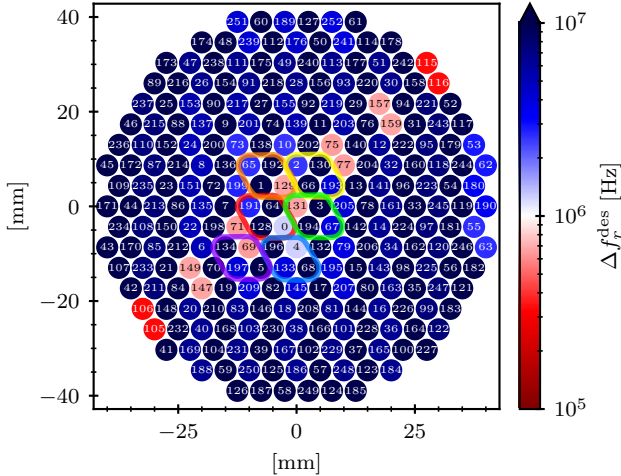


Fig. 9. Implemented MKID shuffling strategy, where each circle represents a resonator. The indices indicate the order in frequency space. The rainbow-colored trapezoids exemplify the shuffling strategy, where the 6 first clusters of 4 elements from the 4 different shuffling groups are shown. The color of each circle indicates the closest spectral distance to the directly neighboring resonators, which can be read out from the accompanying colorbar. By design, the average spacing between spatially neighboring resonators is 12.3 MHz and only 14 (5.5%) resonators are closer than 1 MHz by design.

variations, lithographical limited precision, etc.) and not ab initio cross-talk as can be seen in Fig. 9, where the color of the different resonators indicate the designed spectral distance of immediate neighboring resonators at 5 mm pitch. Finally, the statistics of the 202 usable resonators yield an average internal quality factor of $\overline{Q_i} \approx 1.6 \times 10^5$ and an average coupling quality factor of $\overline{Q_c} \approx 2.3 \times 10^4$.

VI. CONCLUSIONS AND OUTLOOK

In this paper we have shown the design and measurements of spiral inductors Ti/Al lumped element resonators as dual-polarized absorber-coupled MKIDs for millimeter-wavelength

radiation. The electromagnetic design simulations indicate that the lens-coupled spiral absorbers provide a lens aperture efficiency of more than 70% for an octave bandwidth for the 4×4 spiral array absorber and for 10% relative bandwidth for the single spiral absorber. First, a 9 detector chip is fabricated in order to test the two absorber designs. To ensure that only millimeter-wavelength radiation emanating from the calibrated blackbody is captured by the detectors, we designed and fabricated an 85 GHz Nb Fabry-Pérot band-pass filter that sits on one of the lids of a specifically designed chip holder with a $\varnothing 3$ cm aperture and otherwise light-tight. While the spiral array yields a better simulated optical response, we found that the single spiral absorber is more responsive than the spiral array absorber, likely due to the smaller active volume. Nonetheless, both detectors respond about 1 Hz/mK and the PSD, and showcase a loading-dependent quasi-particle roll-off. We give a first estimate of the sensitivity with a NET of $1 \text{ mK}/\sqrt{\text{Hz}}$ at 1 kHz audio frequency, which is on par with other millimeter-wavelength cameras like NIKA [9]. With these findings, we designed and fabricated a millimeter-wavelength 4" camera prototype featuring 253 dual-polarized spiral array MKIDs read out from a single line. Most of the detectors were found (95% detector yield) and 80% of the total detector count were deemed usable (spectrally distant), for which we performed statistics. We report an average internal quality factor of $\overline{Q_i} \approx 1.6 \times 10^5$, an average coupling quality factor of $\overline{Q_c} \approx 2.3 \times 10^4$, a resonance frequency scatter of 5.8% and a mean frequency offset with respect to the design of 5.0%. We attribute these frequency deviations to fabrication imperfections, such as thickness inhomogeneities in the superconducting film and the limited precision of optical lithography.

Follow-up work should characterize the noise equivalent power (NEP) and optical efficiency of these detectors including the lenses following the formalism for multi-moded detectors reported by Dabironezare *et al.* in [5]. To this end, our cryogenic setup must improve its thermal and mechanical

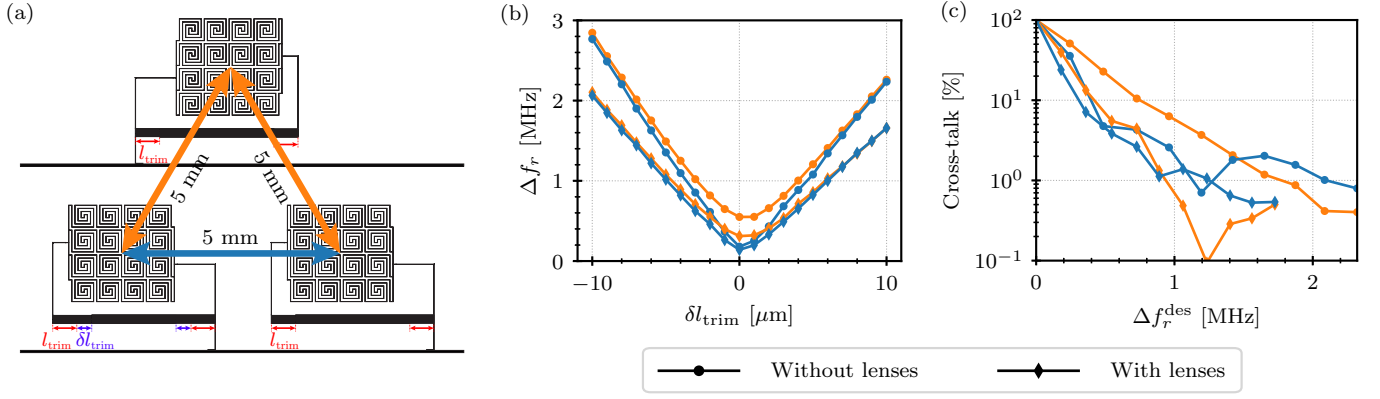


Fig. 10. Cross-talk assessment between neighboring detectors. Sub-figure (a) shows the two possible means of cross-talk between 5 mm-pitched hexagonally-packed spiral array resonators: laterally (blue) or transversely (orange). Sub-figure (b) shows the frequency offset of the two coupled resonators when compared to the isolated one for $\delta l_{\text{trim}} = 0 \mu\text{m}$. Sub-figure (c) quantifies the cross-talk between two neighboring resonators.

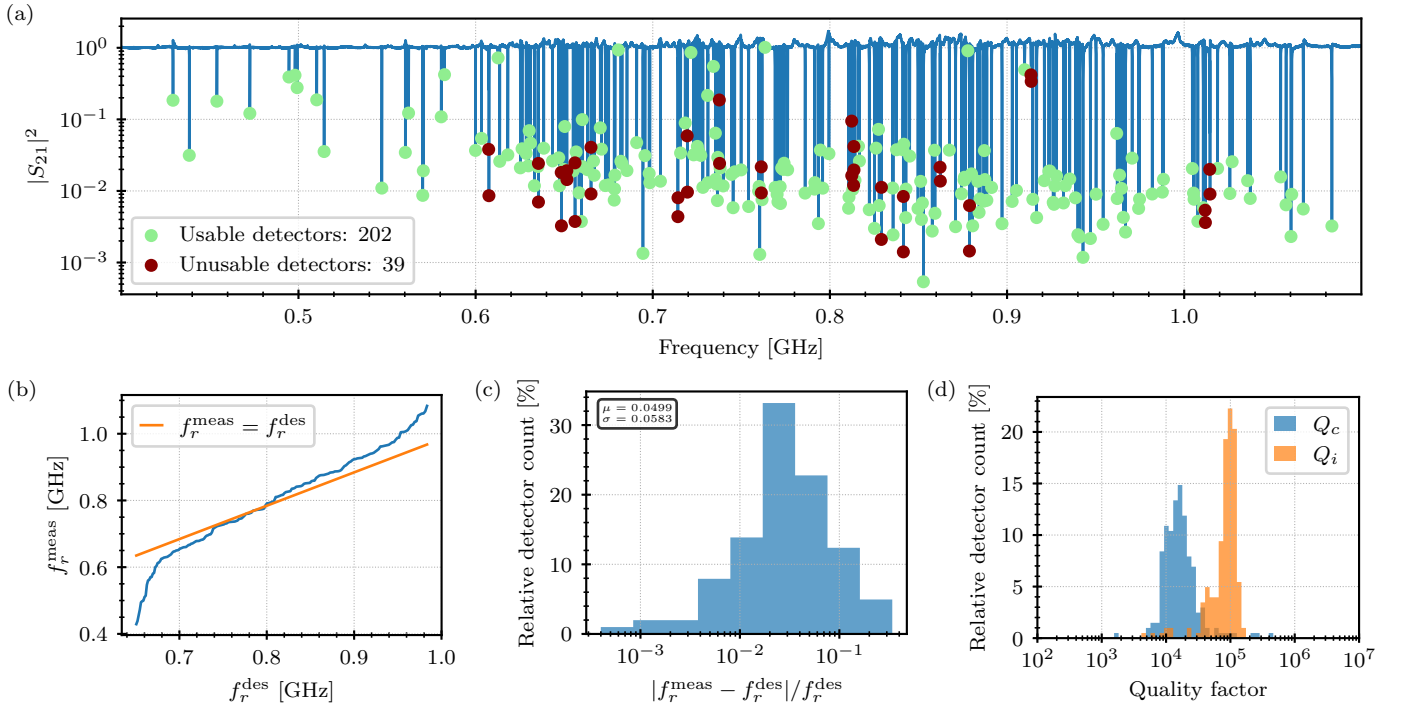


Fig. 11. Panel (a) shows the transmission of the microwave readout of the 253 pixel wafer array measured at 100 mK calibrated out with the transmission measured at 450 mK, where the resonators are too shallow due to the conduction loss. The total number of detected resonators is 241, giving a yield of $241/253 \approx 95\%$. Only the 202 resonators with neighboring resonances further than 20 half-power bandwidths are considered usable. Panel (b) illustrates the measured resonance frequencies as a function of the respective design frequencies. Panel (c) showcases the relative resonance frequency error with respect to the design. Panel (d) contains histograms of the coupling and internal quality factors.

anchoring to reduce the large observed $1/f$ noise. Furthermore, we need to characterize our quasi-optical filters at 4 K and include a box-in-a-box light-tight setup [33] to absolutely quantify the blackbody power impinging on the detectors. Possible improvements in the sensitivity will come from using NbTiN for the capacitors to reduce the stray-light response and noise [30], [34]. An alternative route to lumped-element MKIDs is to employ antenna-coupled ones, where the quasi-optical coupling and detection mechanisms of the MKID can be optimized largely independently from each other.

ACKNOWLEDGMENTS

The authors would like to thank J. J. A. Baselmans, S. O. Dabironezare, J. Martín-Pintado, M. Calvo, and A. Monfardini for the useful discussions and suggestions; and R. Ferrándiz for his support in designing and fabricating the light-tight chip holder.

REFERENCES

- [1] P. K. Day, H. G. LeDuc *et al.*, “A broadband superconducting detector suitable for use in large arrays,” *Nature*, vol. 425, no. 6960, pp. 817–821, Oct. 2003. [Online]. Available: <https://doi.org/10.1038/nature02037>
- [2] J. J. A. Baselmans, F. Facchin *et al.*, “Ultra-sensitive THz microwave kinetic inductance detectors for future space telescopes,” *Astron. Astrophys.*, vol. 665, p. A17, 2022. [Online]. Available: <https://doi.org/10.1051/0004-6361/202243840>
- [3] S. J. C. Yates, A. Pascual Laguna *et al.*, “Demonstration of ultrasensitive kids for future thz space borne polarimeters,” *IEEE Trans. Terahertz Sci. Technol.*, vol. 15, no. 4, pp. 558–565, Jul. 2025.
- [4] P. K. Day, N. F. Cothard *et al.*, “A 25-micrometer single-photon-sensitive kinetic inductance detector,” *Phys. Rev. X*, vol. 14, p. 041005, Oct. 2024. [Online]. Available: <https://link.aps.org/doi/10.1103/PhysRevX.14.041005>
- [5] S. O. Dabironezare, G. Conenna *et al.*, “Lens based kinetic inductance detectors with distributed dual polarised absorbers for far infra-red space-based astronomy,” 2025. [Online]. Available: <https://arxiv.org/abs/2506.03359>
- [6] P. Szypryt, S. R. Meeker *et al.*, “Large-format platinum silicide microwave kinetic inductance detectors for optical to near-ir astronomy,” *Opt. Express*, vol. 25, no. 21, pp. 25 894–25 909, Oct. 2017. [Online]. Available: <https://opg.optica.org/oe/abstract.cfm?URI=oe-25-21-25894>
- [7] P. J. de Visser, S. A. de Rooij *et al.*, “Phonon-trapping-enhanced energy resolution in superconducting single-photon detectors,” *Phys. Rev. Appl.*, vol. 16, p. 034051, Sep. 2021. [Online]. Available: <https://link.aps.org/doi/10.1103/PhysRevApplied.16.034051>
- [8] K. Kouwenhoven, D. Fan *et al.*, “Resolving power of visible-to-near-infrared hybrid β -Ta/Nb-Ti-N kinetic inductance detectors,” *Phys. Rev. Appl.*, vol. 19, p. 034007, Mar. 2023. [Online]. Available: <https://link.aps.org/doi/10.1103/PhysRevApplied.19.034007>
- [9] A. Monfardini, A. Benoit *et al.*, “A dual-band millimeter-wave kinetic inductance camera for the iram 30 m telescope,” *Astrophys. J. Suppl. Ser.*, vol. 194, no. 2, p. 24, May 2011. [Online]. Available: <https://dx.doi.org/10.1088/0067-0049/194/2/24>
- [10] Adam, R., Adane, A. *et al.*, “The NIKA2 large-field-of-view millimetre continuum camera for the 30 m IRAM telescope,” *Astron. Astrophys.*, vol. 609, p. A115, Jan. 2018. [Online]. Available: <https://doi.org/10.1051/0004-6361/201731503>
- [11] J. F. Macías-Pérez, M. Fernández-Torreiro *et al.*, “KISS: Instrument Description and Performance,” *Publications of the Astronomical Society of the Pacific*, vol. 136, no. 11, p. 114505, Nov. 2024. [Online]. Available: <https://dx.doi.org/10.1088/1538-3873/ad8189>
- [12] The CONCERTO Collaboration, Ade, P. *et al.*, “A wide field-of-view low-resolution spectrometer at APEX: Instrument design and scientific forecast,” *Astron. Astrophys.*, vol. 642, p. A60, 2020. [Online]. Available: <https://doi.org/10.1051/0004-6361/202038456>
- [13] K. Lee, J. Choi *et al.*, “GroundBIRD: A CMB Polarization Experiment with MKID Arrays,” *J. Low Temp. Phys.*, vol. 200, no. 5, pp. 384–391, Sep. 2020. [Online]. Available: <https://doi.org/10.1007/s10909-020-02511-5>
- [14] K. R. Dibert, P. S. Barry *et al.*, “Characterization of mkids for cmb observation at 220 ghz with the south pole telescope,” *IEEE Trans. Appl. Supercond.*, vol. 33, no. 5, pp. 1–5, Aug. 2023.
- [15] J. Sayers, C. Bockstiegel *et al.*, “The status of MUSIC: the multiwavelength sub-millimeter inductance camera,” in *Millimeter, Submillimeter, and Far-Infrared Detectors and Instrumentation for Astronomy VII*, W. S. Holland and J. Zmuidzinas, Eds., vol. 9153, International Society for Optics and Photonics. SPIE, 2014, p. 915304. [Online]. Available: <https://doi.org/10.1117/12.2055444>
- [16] B. Aja, S. Arguedas Cuendis *et al.*, “The canfranc axion detection experiment (cadex): search for axions at 90 ghz with kinetic inductance detectors,” *J. Cosmol. Astropart. Phys.*, vol. 2022, no. 11, p. 044, Nov. 2022. [Online]. Available: <https://dx.doi.org/10.1088/1475-7516/2022/11/044>
- [17] Catalano, A., Goupy, J. *et al.*, “Bi-layer kinetic inductance detectors for space observations between 80–120 ghz,” *Astron. Astrophys.*, vol. 580, p. A15, Jul. 2015. [Online]. Available: <https://doi.org/10.1051/0004-6361/201526206>
- [18] G. Wang, P. S. Barry *et al.*, “Electromagnetic properties of aluminum-based bilayers for kinetic inductance detectors,” *IEEE Trans. Appl. Supercond.*, vol. 33, no. 5, pp. 1–6, Aug. 2023.
- [19] M. C. de Ory, D. Rodriguez *et al.*, “Optimized cross-polarized lekids for w-band using sawtooth inductors,” *IEEE Trans. Microw. Theory Tech.*, vol. 72, no. 1, pp. 648–658, Jan. 2024.
- [20] B. A. Mazin, “Superconducting materials for microwave kinetic inductance detectors,” 2020. [Online]. Available: <https://arxiv.org/abs/2004.14576>
- [21] N. Llombart, S. O. Dabironezare *et al.*, “Reception power pattern of distributed absorbers in focal plane arrays: A fourier optics analysis,” *IEEE Trans. Antennas Propag.*, vol. 66, no. 11, pp. 5990–6002, Nov. 2018.
- [22] A. Kusaka, E. J. Wollack, and T. R. Stevenson, “Angular and polarization response of multimode sensors with resistive-grid absorbers,” *J. Opt. Soc. Am. A*, vol. 31, no. 7, pp. 1557–1576, Jul. 2014. [Online]. Available: <https://opg.optica.org/josaa/abstract.cfm?URI=josaa-31-7-1557>
- [23] P. M. Echternach, S. van Berkel *et al.*, “Large array of single-photon counting quantum capacitance detectors,” *IEEE Trans. Terahertz Sci. Technol.*, vol. 12, no. 2, pp. 211–216, Mar. 2022.
- [24] D. Filipovic, S. Gearhart, and G. Rebeiz, “Double-slot antennas on extended hemispherical and elliptical silicon dielectric lenses,” *IEEE Trans. Microw. Theory Tech.*, vol. 41, no. 10, pp. 1738–1749, Oct. 1993.
- [25] J. Bueno, S. Bosma *et al.*, “Lossless matching layer for silicon lens arrays at 500 ghz using laser ablated structures,” *IEEE Trans. Terahertz Sci. Technol.*, vol. 12, no. 6, pp. 667–672, Nov. 2022.
- [26] Dassault Systèmes Simulia Corp., “CST Studio Suite,” 2020. [Online]. Available: <https://www.3ds.com/products-services/simulia/products/cst-studio-suite/>
- [27] D. C. Mattis and J. Bardeen, “Theory of the anomalous skin effect in normal and superconducting metals,” *Physical Review*, vol. 111, no. 2, pp. 412–417, 1958.
- [28] M. C. Diez, T. O. Klaassen *et al.*, “Reflectance measurements on submillimeter absorbing coatings for HIFI,” in *UV, Optical, and IR Space Telescopes and Instruments*, J. B. Breckinridge and P. Jakobsen, Eds., vol. 4013, International Society for Optics and Photonics. SPIE, 2000, pp. 129 – 139. [Online]. Available: <https://doi.org/10.1117/12.393977>
- [29] “QMC Instruments.” [Online]. Available: <https://www.qmcinstruments.co.uk/>
- [30] R. M. J. Janssen, J. J. A. Baselmans *et al.*, “High optical efficiency and photon noise limited sensitivity of microwave kinetic inductance detectors using phase readout,” *Appl. Phys. Lett.*, vol. 103, no. 20, p. 203503, Nov. 2013. [Online]. Available: <https://doi.org/10.1063/1.4829657>
- [31] O. Noroozian, P. K. Day *et al.*, “Crosstalk reduction for superconducting microwave resonator arrays,” *IEEE Trans. Microw. Theory Tech.*, vol. 60, no. 5, pp. 1235–1243, May 2012.
- [32] S. J. C. Yates, J. J. A. Baselmans *et al.*, “Clean beam patterns with low crosstalk using 850 ghz microwave kinetic inductance detectors,” *J. Low Temp. Phys.*, vol. 176, no. 5, pp. 761–766, Sep. 2014. [Online]. Available: <https://doi.org/10.1007/s10909-013-1034-z>
- [33] J. Baselmans, S. Yates *et al.*, “Ultra low background cryogenic test facility for far-infrared radiation detectors,” *Journal of Low Temperature Physics*, vol. 167, no. 3, pp. 360–366, May 2012. [Online]. Available: <https://doi.org/10.1007/s10909-012-0511-0>
- [34] R. Barends, H. L. Hortensius *et al.*, “Noise in nbtin, al, and ta superconducting resonators on silicon and sapphire substrates,” *IEEE Trans. Appl. Supercond.*, vol. 19, no. 3, pp. 936–939, Jun. 2009.